Journal of Power Sources 195 (2010) 6268–6279

Contents lists available at ScienceDirect

Journal of Power Sources

journal homepage: www.elsevier.com/locate/jpowsour

Effect of morphology and space charge on conduction through porous doped ceria

Feng Zhao, Anil V. Virkar*

Department of Materials Science and Engineering, University of Utah, 122 S. Central Campus Drive, Salt Lake City, UT 84112, United States

ARTICLE INFO

Article history:
Received 23 February 2010
Received in revised form 23 April 2010
Accepted 26 April 2010
Available online 20 May 2010

Keywords:
Ceria
Porous materials
Space charge
Conductivity
SOFC
Electrodes

ABSTRACT

Porous samples of samaria (Sm_2O_3)-doped ceria (CeO_2) (SDC) were fabricated using two methods: (1) conventional sintering of powder compacts; and (2) fabrication of sintered NiO + SDC two-phase samples, reduction of NiO to Ni, and acid leaching of Ni. Electrical conductivities of as-fabricated bar samples were measured using a four-probe DC technique. The conductivity of samples made by acid leaching of Ni was up to two orders of magnitude higher than that of conventionally fabricated samples of the same porosity. This difference was attributed to differences in relative inter-particle neck sizes. A simple analytical model was developed to describe conductivity of porous bodies in terms of inter-particle neck sizes. The total electrical conductivity of samples fabricated by the leaching process was measured as a function of oxygen pressure and temperature. The effect of space charge was included in the model describing electrical conduction through porous bodies. The adverse effects of space charge on conductivity are more pronounced in porous ceria as compared to dense ceria.

1. Introduction

Porous ionic and mixed ionic/electronic conductors are of interest for applications such as electrode materials in solid oxide fuel cells [1], gas separation membranes, electrolyzers, and ceramic gas sensors [2,3]. The effective electrical conductivity of porous ceramics is a function of porosity [4,5], grain size, inter-particle neck size, etc. Much of the literature, however, is on conductivity of dense polycrystalline materials. For dense polycrystalline materials, the smaller the grain size, generally the higher is the resistivity (the lower is the conductivity). In many materials, the grain boundary resistivity is several orders of magnitude higher than that of bulk, especially at low temperatures [6–10]. The resistivity of grain boundaries has often been attributed to an intergranular siliceous phase [11,12]. However, even for materials of high purity, the specific grain boundary conductivity measured at low temperatures is still several orders of magnitude lower (specific grain boundary resistivity several orders of magnitude higher) than that of the bulk [13]. This low conductivity of grain boundaries thus cannot be attributed to an intergranular phase. Part of this resistance, however, may be attributable to space charge effects, which tend to lower the charge carrier concentrations near grain boundaries in some materials. Frenkel [14] was the first to propose the existence of space charge. Its mathematical analysis and implications concerning conductivity in alkali halides were presented by Lehovec [15]. Detailed thermodynamic analysis using energy minimization was presented by Kliewer and Koehler [16]. Subsequently, many researchers have analyzed the existence of space charge in other ionic compounds, although the basic formalism is essentially the same as given by Lehovec [15] and Kliewer and Koehler [16].

Recent work by Guo [17,18] has shown that in yttria-stabilized zirconia (YSZ) at low temperatures, the high grain boundary resistivity may be attributed to a space charge region, which results from the depletion of oxygen vacancies near grain boundaries. Some researchers have also reported on the effect of space charge on conduction mechanism in polycrystalline cerium oxide. Kim and Maier [19], for example, have investigated the conductivity of nanocrystalline ceria and concluded that the space charge effect leads to a high grain boundary resistivity. Tschöpe [20,21] investigated electrical transport properties of nanocrystalline and microcrystalline ceria as a function of temperature and oxygen partial pressure. It was concluded that the electronic conductivity of nanocrystalline ceria increases with decreasing grain size. Earlier work by Guo et al. also investigated grain boundaries in yttria-doped and undoped ceria [22]. The authors concluded that the blocking effect of grain boundaries in high purity ceria may be attributed to the existence of a positive space charge potential caused by the depletion of oxygen vacancies, similar to that in zirconia. Tschöpe et al. [23] calculated the electrical conductivity of mesoscopic cubic cerium oxide crystals with space charge layers as a function of grain size. They found that the electronic conductivity decreases with increasing grain size, and the ionic conductivity increases with increasing grain size. Lubomirsky et al. [24] modeled the distribution of mobile charge carriers in the space charge region of grain boundaries. They found that the depletion effects are more pronounced at edges and corners due to geometry.

* Corresponding author. Tel.: +1 801 581 5396; fax: +1 801 581 4816.
E-mail address: anil.virkar@m.cc.utah.edu (A.V. Virkar).

0378-7753/$ – see front matter © 2010 Elsevier B.V. All rights reserved.
doi:10.1016/j.jpowsour.2010.04.079

Nomenclature

$[A']_b$	Acceptor concentration in the bulk
d	Grain size
e	Electronic charge
p_{O_2}	Oxygen partial pressure
R	Particle radius
r_0	Neck radius
R_I	Resistance of region I
R_{II}	Resistance of region II
R_{III}	Resistance of region III
R_{eff}	Effective resistance
T	Absolute temperature
k_B	Boltzmann's constant
n	Electron concentration
$N_j(x)$	Concentration of species j at distance x from the grain boundary core
$[V_O^{\bullet\bullet}]$	Oxygen vacancy concentration
V_v	Volume fraction porosity
z_i	Valence of i

Greek letters

$\alpha = r_0/R$	relative neck size
ε_0	Permittivity of free space
ε_r	Dielectric constant
λ	Debye length
λ^*	Space charge layer width
θ	Half the angle of the cone with $2r_0$ as the base and apex at the center of the particle
δ_{gb}	Grain boundary core width
μ_e	Electron field mobility
$\mu_{V_O^{\bullet\bullet}}$	Oxygen vacancy field mobility
ρ	Resistivity
ρ_{eff}	Effective resistivity
ΔH°	Enthalpy
$\Delta\phi(x)$	Electrostatic potential difference

The studies on space charge in ionic crystals reported to date have been on dense materials. In the space charge model, a grain boundary consists of a grain boundary core (crystallographic mismatch region) and two adjacent space charge layers as described by Maier [25]. Typical electrodes in electrochemical devices such as fuel cells and oxygen separation membranes are porous materials. In such cases, both ion transport and electron/hole transport through the solid regions of porous electrodes can have a profound effect on the overall performance of membranes. Thus, ionic and electronic conduction through porous materials is of particular interest in such devices. The effects of grain boundaries and space charge are expected to be important with the additional effects related to porosity and morphology. The present work is on the investigation of conductivity of porous bodies. In porous materials, in addition to volume fraction porosity and particle size, an important factor concerns the morphology – which mainly includes the nature of inter-particle contacts.

Yttria-doped zirconia (YSZ) and rare earth oxide doped cerium oxide are two of the most widely used electrolyte materials for solid state electrochemical devices, for example, solid oxide fuel cells, oxygen separation membranes, steam electrolyzers and sensors. YSZ is an essentially pure ionic conductor over a wide range of temperatures and oxygen partial pressures (p_{O_2}). However, doped ceria is an electron and an oxygen ion mixed conductor. At high temperatures and at low p_{O_2}, it exhibits predominantly n-type conductivity. At high p_{O_2} and low temperatures, it is a predominantly an oxygen ion conductor.

In this manuscript, a simple analytical model to describe the role of connectivity on electrical conductivity of porous bodies, including the effects of grain boundaries and space charge, is presented. The model developed accounts for transport through three regions: the bulk of the grain, the space charge region, and the structural part of the grain boundary. Doped ceria is chosen as a model material. The model also incorporates the effect of p_{O_2} on carrier concentrations in the space charge layer and in the bulk, and their effects on the resistivity of the space charge layer and the bulk. The effective resistivity of porous doped ceria was calculated as a function of grain size and neck size for a given p_{O_2} and temperature.

Porous bar-shaped samples of samaria doped ceria (SDC) with 10 mol.% Sm_2O_3 were fabricated using two methods: (1) a conventional method comprising sintering of SDC powder compacts and (2) sintering a two-phase mixture of SDC + NiO to near full density, reduction of NiO to Ni in flowing hydrogen at elevated temperatures, and acid leaching of Ni at room temperature to form porous SDC. The former approach led to the formation of porous SDC with narrow inter-particle necks. The latter approach led to the formation of porous SDC with wide inter-particle necks. Electrical conductivity of porous SDC bars was measured in air using a four-probe DC technique. The electrical conductivity of some of the porous SDC samples fabricated using the leaching process was also measured as a function of temperature and oxygen partial pressure.

2. Model

2.1. Effective resistivity of a porous body: no space charge effects included

A porous body is modeled as a one-dimensional array of cut spheres with contact area corresponding to the neck size. Fig. 1(a) shows two idealized truncated spherical grains with a grain bound-

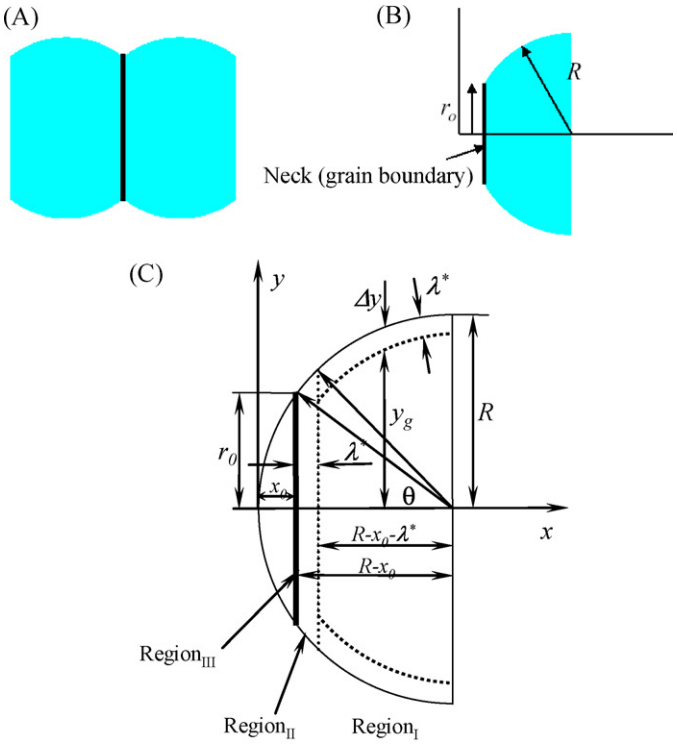

Fig. 1. (a) A schematic representation of two contacting grains, with a grain boundary in between. (b) A schematic representation of a half of the grain with half of the grain boundary associated with it. This is the geometry used in the calculations. (c) Geometry of the particle used for calculations with space charge effect included.

ary in between. Fig. 1(b) shows half of a grain of radius R and neck radius r_0 with half of the grain boundary associated with it. This geometry was used in the calculations. The effective resistivity (see Appendix A) as a function of the relative neck size $\alpha = r_0/R$ and grain radius, R, is approximately given by

$$\rho_{\text{eff}} \approx \frac{2\rho_g}{\pi\sqrt{1-\alpha^2}} \ln\left[\frac{1+\sqrt{1-\alpha^2}}{1-\sqrt{1-\alpha^2}}\right] + \frac{2\rho_{gb}\delta_{gb}}{\pi R\alpha^2\sqrt{1-\alpha^2}} \quad (1)$$

where R is the radius of the particle, which is assumed to be a grain; r_0 radius of the inter-particle neck; $\alpha = r_0/R$ relative neck size; ρ_g grain resistivity without the space charge effect (Ω cm); $\rho_{gb}\delta_{gb}$ is the grain boundary area specific resistance (Ω cm^2). This only refers to the structural part of a grain boundary.

Eq. (1) is approximate and is deemed valid only for values of α not too large; valid for $\alpha < 0.5$.

2.2. Effective resistivity of a porous body: space charge effects included

The geometry of the particle used for calculations is shown in Fig. 1(c). It consists of half of the grain with half of the grain boundary associated with it and includes the space charge layer. The net resistance is divided into three regions: (1) Region I corresponds to the net resistance for the range between $x = x_0 + \lambda^*$ and $x = R$. The corresponding resistance is R_I. (2) Region II corresponds to the net resistance for the range $x = x_0$ and $x = x_0 + \lambda^*$. The corresponding resistance is R_{II}. (3) Region III corresponds to the transport across the grain boundary core. The effective resistance, which includes the effects of space charge, grain boundary and the neck morphology, is given by (see Appendix B):

$$R_{\text{eff}} = R_I + R_{II} + R_{III} \quad (2)$$

where

$$R_I = \int_{\cos^{-1}\left(\frac{R-x_0-\lambda^*}{R}\right)}^{\frac{\pi}{2}} \frac{\rho_g\rho_{sc}\ R\sin^3\theta\, d\theta}{[\pi(2R\lambda^*\sin^2\theta - \lambda^{*2})\rho_g + \pi(R\sin^2\theta - \lambda^*)^2\rho_{sc}]} \quad (3)$$

$$R_{II} = \int_{\cos^{-1}\left(\frac{R-x_0}{R}\right)}^{\cos^{-1}\left(\frac{R-x_0-\lambda^*}{R}\right)} \frac{\rho_{sc}d\theta}{\pi R\sin\theta} \quad (4)$$

and

$$R_{III} = R_{gb} = \frac{\rho_{gb}\delta_{gb}}{2\pi r_0^2} = \frac{\rho_{gb}\delta_{gb}}{2\pi(R\sin\theta)^2} \quad (5)$$

where θ is the angle describing the neck region given by half the angle of the cone formed by the neck with the apex at the center of the grain.

$$\theta = \cos^{-1}\left(\frac{\sqrt{(R^2 - r_0^2)}}{R}\right) = \sin^{-1}\left(\frac{r_0}{R}\right) = \sin^{-1}\alpha \quad (6)$$

where λ^* is the width of the space charge region. For simplicity, it is assumed that in this region, the conductivity is uniform. ρ_{sc} is the resistivity in the space charge region (Ω cm). This may be higher or lower than the grain resistivity. $\rho_{gb}\delta_{gb}$ is the grain boundary area specific resistance (Ω cm^2) as before. This is only the part associated with the structural disorder of a grain boundary.

The typical particle size, R, is in the micron range, the grain boundary thickness is in the fractions of a nanometer range, and the space charge width, λ^* is estimated to be in fractions of a nanometer to even tens of nanometers, depending upon dopant concentration and temperature. Thus, we expect that $R > \lambda^* \geq \delta_{gb}$ and typically $R \gg \lambda^* \geq \delta_{gb}$.

R_{eff}: The net resistance of half of a grain with half of a grain boundary associated with it.

Based on the assumption that the grains (or particles) are arranged on a square lattice, the effective resistivity of such a material can be computed by the following equation:

$$\rho_{\text{eff}} \approx \frac{4R_{\text{eff}}R^2}{R - x_0} = \frac{4R_{\text{eff}}R}{\cos\theta} \quad (7)$$

In this calculation the effect of curvature was neglected and the equi-potential lines were assumed to be straight, parallel to the grain boundary.

2.3. Approximate estimate of porosity

For the idealized model used here, the fractional porosity is given by

$$V_v \approx \frac{\cos^2\ \theta}{3} \quad (8)$$

For $\theta = 0^\circ$, the porosity is 0.333 or 33.3%; for $\theta = 20^\circ$, the porosity is 0.294 or 29.4%; and for $\theta = 30^\circ$, the porosity is 0.25 or 25%. Thus, over a wide range of neck sizes, the porosity is approximately constant (at ~25–30%). For the highest value of $\theta = 45^\circ$ used in the calculations, the porosity is ~17%. Thus, for much of the range of neck sizes investigated, the porosity is nearly constant, except for the highest values of θ used in the model.

2.4. Resistivity in the bulk and in the space charge layer in doped ceria

All defects are assumed to be in thermodynamic equilibrium. Doped ceria is chosen here as a model material. Doped ceria is known [26–29] to be a mixed conductor of oxygen ions and electrons, depending upon the oxygen partial pressure and temperature. Acceptor doping creates oxygen vacancies by a defect reaction of the type:

$$A_2O_3 \rightarrow 2A' + V_O^{\cdot\cdot} + 3O_O^\times \quad (9)$$

At elevated temperatures and low oxygen partial pressures, electrons and oxygen vacancies can be generated by a reaction of the type:

$$O_O^\times \rightarrow 2e' + V_O^{\bullet\bullet} + \tfrac{1}{2}O_2 \quad (10)$$

The corresponding law of mass action can be expressed as

$$n^2[V_O^{\bullet\bullet}] = k\exp\left[-\frac{\Delta H^\circ}{k_BT}\right] p_{O_2}^{-1/2} \quad (11)$$

where n is the electron concentration, $[V_O^{\bullet\bullet}]$ is the oxygen vacancy concentration, k is a constant, ΔH° is the enthalpy of reaction (10), k_B the Boltzmann constant, and p_{O_2} is the oxygen partial pressure in the atmosphere.

According to the condition of electroneutrality, the concentrations of $V_O^{\bullet\bullet}$ in the bulk can be expressed as

$$[V_O^{\bullet\bullet}]_b = \frac{[A']_b + n}{2} \quad (12)$$

The dopant concentration in the bulk $[A']_b$, the p_{O_2} and the temperature T are given by the experimental conditions. For cerium oxide, $k = 1.2 \times 10^{74}$ and $\Delta H^\circ = 4.67$ eV [30]. From Eqs. (11) and (12) the defect concentrations (oxygen vacancies and electrons) in the bulk can be calculated as a function of temperature and oxygen partial pressure.

The total electrical conductivity for doped ceria is a sum of the ionic conductivity and the electronic conductivity, given by

$$\sigma = 2e[V_O^{\bullet\bullet}]\mu_{V_O^{\bullet\bullet}} + en\mu_e \quad (13)$$

where the electrical field mobilities of oxygen vacancies and electrons are respectively $\mu_{V_O^{\bullet\bullet}}$ and μ_e in $cm^2\,V^{-1}\,s^{-1}$. Then the total conductivity in the bulk can be expressed as

$$\sigma_b = \sigma_{i(bulk)} + \sigma_{e(bulk)} = 2e[V_O^{\bullet\bullet}]_b \mu_{V_O^{\bullet\bullet}} + en_b\mu_e \quad (14)$$

where $[V_O^{\bullet\bullet}]_b$ and n_b are concentrations in the bulk. Then the total resistivity in the bulk can be written as

$$\rho_b = \frac{1}{\sigma_b} = \frac{1}{2e[V_O^{\bullet\bullet}]_b \mu_{V_O^{\bullet\bullet}} + en_b\mu_e} \quad (15)$$

For ceria, the electron mobility as a function of temperature is given by [30]:

$$\mu_e(T) = \frac{3.9\times10^2}{T}\exp\left[-\frac{4.63\times10^3}{T}\right] \quad (16)$$

and the mobility of oxygen vacancies as a function of temperature is given by [31]:

$$\mu_{V_O^{\bullet\bullet}}(T) = \frac{2.92\times10^2}{T}\exp\left[-\frac{7.84\times10^3}{T}\right] \quad (17)$$

At equilibrium, the electrochemical potentials of mobile species are spatially invariant. Thus, the concentration $N_j(x)$ of any defect j with charge $z_j e$ in the space charge layer in the dilute solution limit is given as [15,16]:

$$\frac{N_j(x)}{N_j(\text{bulk})} = \exp\left[-\frac{z_j e\Delta\phi(x)}{k_B T}\right] \quad (18)$$

where x is the distance from the interface between the grain boundary core and the space charge layer; $\Delta\phi(x)$ is the electrostatic potential referenced to the bulk, i.e., the so-called space charge potential. By solving Poisson's equation, the $\Delta\phi(x)$ is related to the dopant concentration and the space charge layer thickness by (for $x<\lambda^*$) [32]:

$$\Delta\phi(x) \approx \frac{e[A']_b}{\varepsilon_0\varepsilon_r}(x-\lambda^*)^2 \quad (19)$$

where $[A']_b$ is the dopant concentration in the bulk in $\#cm^{-3}$, ε_0 is the permittivity of free space, ε_r is the dielectric constant, and λ^* is the space charge layer thickness. The Debye length, λ, and the space charge layer width, λ^*, are given by [32]:

$$\lambda = \sqrt{\frac{k_B T\varepsilon_0\varepsilon_r}{4e^2[A']_b}} \quad (20a)$$

and

$$\lambda^* = \lambda\sqrt{\frac{4e}{k_B T}\Delta\phi(0)} \quad (20b)$$

where $\Delta\phi(0)$ is the space charge potential at the grain boundary. For ceria the dielectric constant is given by $\varepsilon_r = 26$ [33]. The electron and oxygen vacancy concentrations in the space charge layer can be expressed respectively as

$$n_{(x)} = n_b\exp\left[\frac{e\Delta\phi(x)}{k_B T}\right] \quad (21)$$

and

$$[V_O^{\bullet\bullet}]_{(x)} = [V_O^{\bullet\bullet}]_b\exp\left[-\frac{2e\Delta\phi(x)}{k_B T}\right] \quad (22)$$

Then the specific conductivity in the space charge layer at a distance of x from the grain boundary core is given by

$$\sigma_{sc(x)} = 2e[V_O^{\bullet\bullet}]_{(x)}\mu_{V_O^{\bullet\bullet}} + en_{(x)}\mu_e \quad (23)$$

The average electronic conductivity in the space charge layer can be given as

$$\sigma_{e(sc)} = \frac{1}{\frac{1}{\lambda^*}\int_0^{\lambda^*}\frac{1}{\sigma_e(x)}\,dx} \quad (24)$$

Inserting Eqs. (19)–(21) into Eq. (24) and rearranging

$$\sigma_{e(sc)} = \frac{e\mu_e n_b\lambda^*}{\int_0^{\lambda^*}\exp\left[-\frac{e^2[A']_b}{\varepsilon_o\varepsilon_r k_B T}(x-\lambda^*)^2\right]dx} = \sigma_{e(bulk)}\frac{\lambda^*}{\int_0^{\lambda^*}\exp\left[-\frac{e^2[A']_b}{\varepsilon_o\varepsilon_r k_B T}(x-\lambda^*)^2\right]dx} \quad (25)$$

Similarly, the average ionic conductivity in the space charge layer can be given as

$$\sigma_{i(sc)} = \frac{1}{\frac{1}{\lambda^*}\int_0^{\lambda^*}\frac{1}{\sigma_i(x)}dx} \quad (26)$$

Inserting Eqs. (19), (20) and (22) into Eq. (26) and rearranging

$$\sigma_{i(sc)} = \frac{2e\mu_{V_O^{\bullet\bullet}}[V_O^{\bullet\bullet}]_b\lambda^*}{\int_0^{\lambda^*}\exp\left[\frac{z_i e^2[A']_b}{\varepsilon_0\varepsilon_r k_B T}(x-\lambda^*)^2\right]dx} = \sigma_{i(bulk)}\frac{\lambda^*}{\int_0^{\lambda^*}\exp\left[\frac{z_i e^2[A']_b}{\varepsilon_0\varepsilon_r k_B T}(x-\lambda^*)^2\right]dx} \quad (27)$$

Thus, the average resistivity in the space charge region including oxygen ions and electrons can be given by

$$\rho_{sc} = \frac{1}{\sigma_{sc}} = \frac{1}{\sigma_{e(sc)} + \sigma_{i(sc)}} \quad (28)$$

3. Experimental

3.1. Fabrication and conductivity measurement of porous samaria doped ceria (SDC) samples with widely varying morphologies (neck sizes)

Two different methods were used to make samples of various porosities. The main objective was to fabricate samples with various neck sizes; from narrow necks to wide necks. In the first method, powder compacts were formed by die-pressing SDC powder containing 10 mol.% Sm_2O_3–90 mol.% CeO_2 followed by iso-static pressing. The samples were sintered in air over a range of temperatures between ~1200 °C and ~1600 °C to achieve varying porosity levels. Depending upon the degree of sintering achieved, this method is also expected to yield samples with varying particle (grain) and neck sizes.

The process used for making the second group of samples was as follows: powder mixtures of commercial NiO and in-house combustion-synthesized SDC in various NiO:SDC weight ratios corresponding to 20:80, 30:70 and 40:60 were wet-milled, dried, and then screened. Bar-shaped powder compacts were formed by die-pressing followed by iso-static pressing. The samples were sintered in air at 1600 °C for 2 h. The sintered samples were then reduced in a flowing 10% hydrogen + nitrogen gas mixture for 2 h at 800 °C, followed by a treatment in 100% hydrogen, also at 800 °C for 2 h. This led to the reduction of NiO to Ni. Finally the reduced bar samples were leached in a dilute nitric acid solution for 3 h at room temperature. This led to the removal of Ni as $Ni(NO_3)_2$, and created additional porosity. The resulting samples were single-phase, porous SDC. NiO and SDC have negligible solubility in each other. Thus, the resulting SDC samples have negligible NiO dissolved in the lattice of SDC.

The total conductivity of the two groups of samples with different porosity levels was measured in air over a range of temperatures by a four-probe DC method. Prior to the measurement of conductivity, all samples were thermally treated in air at 1200 °C for 4 h. The objective was to ensure that the same grain boundary structure and characteristics (such as dopant segregation) would be established at the grain boundaries in all samples, regardless of porosity, particle size and the initial sintering conditions. After testing, fractured pieces of each sample were impregnated with an epoxy. Upon curing and hardening the epoxy, the samples were mounted in a plastic mount, and subsequently polished to a 1 μm finish. The samples were then examined under a scanning electron microscope (SEM). The microstructures of porous samples were characterized by quantitative stereology to estimate the porosity.

3.2. Conductivity measurement of porous SDC samples as a function of oxygen partial pressure and temperature

The total conductivity of porous SDC samples fabricated using the leaching process was measured as a function of oxygen partial pressure, p_{O_2}, and temperature using a four-probe DC technique. The p_{O_2} was varied between $\sim 10^{-15}$ atm and 1 atm. For obtaining p_{O_2} higher than 10^{-5} atm, O_2–N_2 gas mixtures were used. Lower oxygen partial pressures were achieved using H_2/H_2O gas mixtures. The p_{O_2} was monitored using a zirconia potentiometric oxygen sensor. After the measurement at 600 °C, the sample was heated to higher temperatures for making further conductivity measurements.

4. Results and discussion

4.1. Effect of neck size on the effective resistivity of a porous conductor (no space charge effects included)

Eq. (1) shows that the effective resistivity of a porous conductor depends on the grain resistivity, ρ_g, the grain boundary resistivity parameter, namely $\rho_{gb}\delta_{gb}$, and the relative neck size α, given by $\alpha = r_0/R$. Of particular interest is to determine the relative contributions of the two terms in Eq. (1) as a function of α for small values of α. It is readily shown that as $\alpha \to 0$, Eq. (1) can be approximately given by

$$\rho_{eff} \approx \frac{4}{\pi}\rho_g \ln\left(\frac{2}{\alpha}\right) + \frac{2\rho_{gb}\delta_{gb}}{\pi R\alpha^2} \quad (29)$$

As seen from Eq. (29), as $\alpha \to 0$, both terms become infinite. One can use l'Hospital's rule to show that the second term goes to infinity faster than the first term. The ratio of the derivative of the second term to the derivative of the first term varies as $1/\alpha^2$. This result has significant implications concerning the resistivity of porous bodies, especially the role of grain boundaries. Eq. (29) shows that a poorly sintered porous conductor (with narrow necks) will exhibit high effective resistivity with a relatively larger contribution from grain boundary resistance than a fully dense material. Thus, the effect of grain boundaries on ρ_{eff} is disproportionately high in porous bodies due mainly to small neck sizes. This is true no matter what the grain boundary resistivity is – as long it is nonzero. That is, even in materials with low grain boundary resistivity, the effect of grain boundaries is more pronounced in porous materials as compared to dense materials. This effect is related to the constriction.

4.2. Effect of morphology and space charge on the effective resistivity of porous doped ceria

For $T = 600$ °C (873 K), $p_{O_2} = 0.21$ atm, doping level = 10% (corresponding $[A']_b = 2.686 \times 10^{21}$ cm^{-3}, $\left[V_O^{\bullet\bullet}\right]_b = 1.34 \times 10^{21}$ cm^{-3}, and $n_b = 1.86 \times 10^{14}$ cm^{-3} where n_b was estimated from Eq. (11)), space charge potential $\Delta\phi(0) = 0.4$ V [22], and using Eqs. (20a) and (20b) the Debye length and the space charge layer thickness are estimated to be 0.1 nm and 0.4 nm, respectively. Note that because of the high dopant concentration, the Debye and space charge lengths are only a fraction of a nanometer. Using Eqs. (25) and (27), the average electronic and ionic conductivities in the space average layer in terms of the corresponding bulk values at 600 °C are estimated as

$$\sigma_{e(sc)} \approx 2.5\sigma_{e(bulk)} \quad (30)$$

and

$$\sigma_{i(sc)} \approx 0.005\sigma_{i(bulk)} \quad (31)$$

The above shows that the ionic conductivity in the space charge layer is considerably lower compared to the value in the bulk. The resistivity in the space charge layer is thus estimated as

$$\rho_{sc} = \frac{1}{\sigma_{i(sc)} + \sigma_{e(sc)}} = \frac{1}{0.005\sigma_{i(bulk)} + 2.5\sigma_{e(bulk)}} \quad (32)$$

The total conductivity in the bulk, consisting of ionic conductivity in the bulk, $\sigma_{i(bulk)}$ and the electronic conductivity in the bulk, $\sigma_{e(bulk)}$, can be calculated using Eq. (14). Similarly, the average resistivity in the space charge layer can be calculated using Eq. (32).

A similar approach is used to estimate the average resistivity (or conductivity) in the bulk and in the space charge layer as a function of temperature and oxygen partial pressure. Using the calculated bulk conductivity and the average space charge conductivity as a function of temperature and oxygen partial pressure, and using Eqs. (3), (4), (5) and (7), the effective resistivity (or conductivity) of porous ceria was estimated.

Fig. 2 shows the calculated effective resistivity of half of a grain with half of a grain boundary (representing porous doped ceria) as a function of grain size and neck size at 600 °C and $p_{O_2} = 0.21$ atm using the following parameters: $\rho_g = 52\ \Omega$ cm (Eq. (14)), $\rho_{sc} = 1.06 \times 10^4\ \Omega$ cm (Eq. (28)), $\rho_{gb} = {}^1 50\ \Omega$ cm, $\lambda^* = 0.4$ nm, and $\delta_{gb} = 0.4$ nm [33]. Note that the effective resistivity rapidly rises for small grains and narrow necks. The effective resistivities of porous samples with 0.5 μm grain size in the case of $\theta = 5°$ (narrow neck size) and $\theta = 45°$ (wide neck size) are $3.25 \times 10^3\ \Omega$ cm and $1.77 \times 10^2\ \Omega$ cm, respectively. The effective resistivities of porous samples with a 5 μm grain size in the case of $\theta = 5°$ and 45° are $6.46 \times 10^2\ \Omega$ cm and $1.09 \times 10^2\ \Omega$ cm, respectively. It is seen that the effective resistivity for a sample of 0.5 μm grain size is over 18 times greater for the case of $\theta = 5°$ as compared to that for $\theta = 45°$. Also the effective resistivity for a sample of 5 μm grain size is over 6 times greater for the case of $\theta = 5°$ as compared to that for $\theta = 45°$ angle. The rapid rise in the net resistance at small angles (narrow neck sizes) underscores the importance of good particle to particle contact in porous bodies.

The corresponding parameters at 800 °C and $p_{O_2} = 0.21$ are: $\rho_g = 12\ \Omega$ cm (Eq. (14)), $\rho_{sc} = 2.41 \times 10^3\ \Omega$ cm (Eq. (28)), $\rho_{gb} = 10\ \Omega$ cm, $\lambda^* = 0.4$ nm, and $\delta_{gb} = 0.4$ nm. The ratios of the resistivities are $\rho_g(600\,°C)/\rho_{sc}(600\,°C) = 52/1.06 \times 10^4 = 0.0491$ and $\rho_g(800\,°C)/\rho_{sc}(800\,°C) = 12/2.41 \times 10^3 = 0.0498$. That is the ratio of the grain resistivity to the space charge layer resistivity is virtually the same at 600 °C and 800 °C. As a result, the shapes of the ρ_{eff} vs.

[1] As the grain boundary core has a disordered structure, it is usually assumed that the activation enthalpy and entropy of migration should be much lower in the grain boundary core than those of bulk and space charge layers [17]. Thus, the resistivity in the grain boundary core should be lower than that of bulk and space charge layer. In the present analysis, a value of lower resistivity was assumed and used for the calculation of effective resistivity.

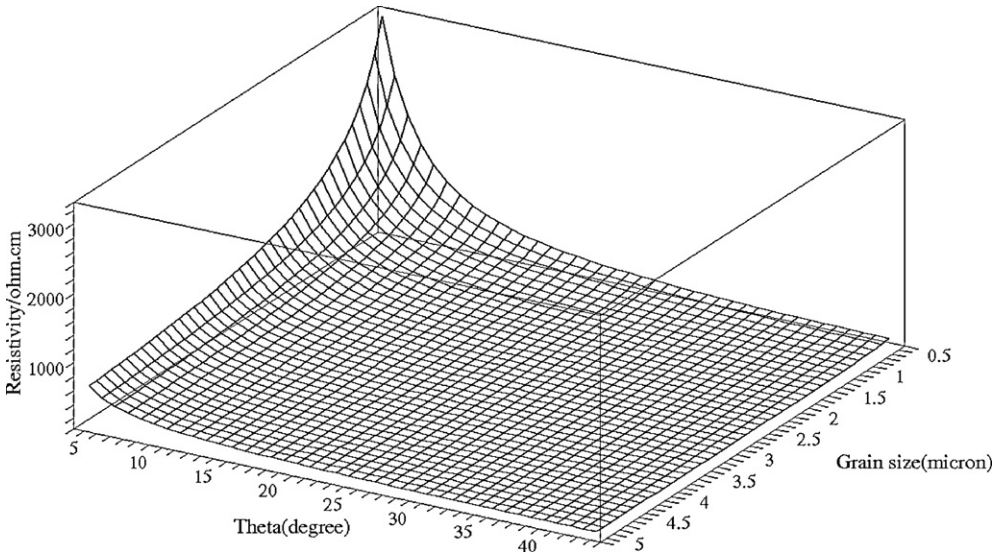

Fig. 2. Effective resistivity (linear scale) of a porous body calculated using half a grain (with half a grain boundary) as a function of angle (relative neck size) and grain size at 600 °C, $p_{O_2} = 0.21$ atm.

θ and grain size $d = 2R$ plots are nearly similar at 600 °C and 800 °C except for the absolute values. Thus, only one at 600 °C is shown here.

4.3. Conductivity and porosity of porous SDC samples

Table 1 shows porosity as a function of sintering conditions for porous samples fabricated using the conventional method and the measured four-probe DC conductivity in air as a function of temperature. Table 2 shows porosity as a function of sintering conditions for porous samples made using Ni-SDC cermets wherein the porosity was created by leaching away Ni, and the measured four-probe DC conductivity in air as a function of temperature. Sintering of SDC powder compacts at 1600 °C resulted in dense samples with ~4.2% porosity, all of which was closed porosity. The grain size of the dense sample was ~7 μm. The corresponding scanning electron micrograph (SEM) is shown in Fig. 3. SDC powder compacts sintered at 1400 °C and 1200 °C exhibited porosity levels of 33.5% and 51.2%, respectively. A large fraction of the porosity in these samples was open. Also, as seen in the corresponding SEMs in Figs. 4 and 5, the inter-particle (inter-grain) necks are small and the grain size is also much smaller than in the dense sample.

In the second group of samples using sintered NiO + SDC compacts, NiO and SDC grains grow simultaneously and form space-filling regular polyhedra (tetrakaidecahedra) which form contiguous and interpenetrating skeletons. Samples greater than 95% theoretical density were made. The NiO and SDC skeletons in the composite form two contiguous phases with large neck sizes (which are essentially SDC-to-SDC, SDC-to-NiO and NiO-to-NiO inter-grain facets). After reducing NiO to Ni and leaching it away, samples with the preferred microstructures of high porosity and large neck sizes were obtained. Figs. 6–8 are SEM micrographs of samples with porosity ranging between 31.2% and 54.8%. These SEM micrographs show good inter-grain connectivity compared to those sintered using the conventional method given in Figs. 4 and 5.

The results of conductivity measurements listed in Tables 1 and 2 show that the effect of microstructure on the effective conductivity is rather large. Fig. 9 shows plots of the normalized conductivity as a function of porosity for the two sets of samples. The normalized conductivity is defined here as the

Table 1
Porosity and conductivity as functions of sintering conditions. Samples fabricated by the conventional method.

SDC (Ce/Sm = 90/20)	Sintered at 1600 °C/4 h	Sintered at 1400 °C/4 h	Sintered at 1200 °C/4 h
Porosity	4.2%	33.5%	51.2%
Conductivity (S cm^{-1})			
650 °C	0.027	0.012	5.18×10^{-5}
700 °C	0.037	0.017	1.19×10^{-4}
750 °C	0.056	0.025	2.52×10^{-4}
800 °C	0.071	0.032	4.31×10^{-4}

Table 2
Porosity and conductivity as functions of sintering conditions. Samples fabricated by the reducing-leaching method.

SDC (Ce/Sm = 90/20)	Sintered at 1600 °C/2 h	Sintered at 1600 °C/2 h	Sintered at 1600 °C/2 h
Porosity	31.2%	39.7%	54.8%
Conductivity (S cm^{-1})			
650 °C	0.016	0.015	0.010
700 °C	0.025	0.024	0.016
750 °C	0.036	0.035	0.023
800 °C	0.051	0.049	0.033

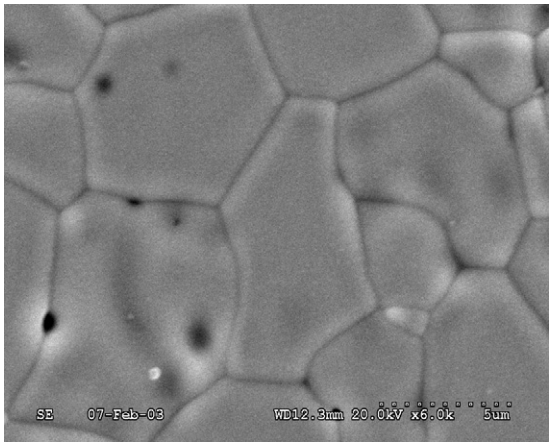

Fig. 3. An SEM micrograph of a Sm_2O_3-doped ceria (SDC) sample (porosity = 4.2%) sintered at 1600 °C/4 h. Note the relatively coarse grain size. Conductivity data are given in Table 1.

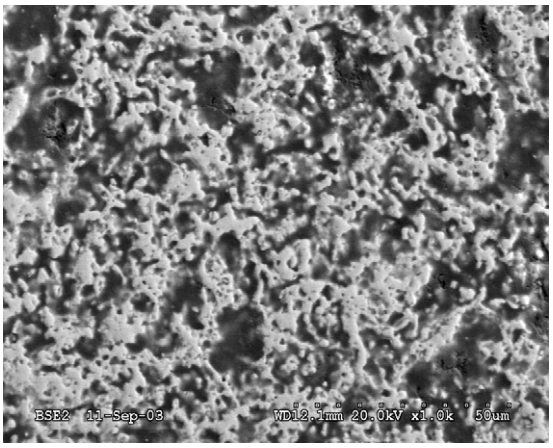

Fig. 4. An SEM micrograph of a Sm_2O_3-doped ceria (SDC) sample (porosity = 33.5%) sintered at 1400 °C/4 h (conventional method). Conductivity data are given in Table 1.

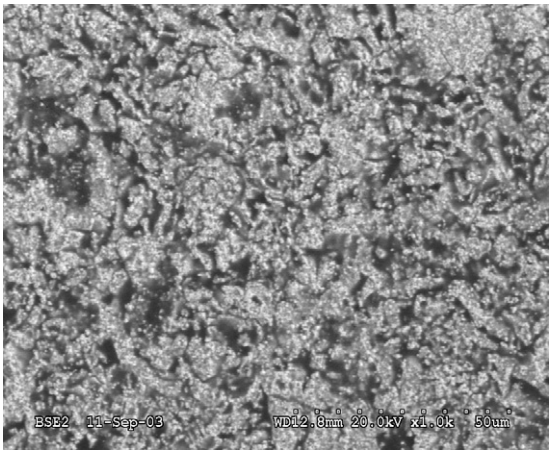

Fig. 5. An SEM micrograph of a Sm_2O_3-doped ceria (SDC) sample (porosity = 51.2%) sintered at 1200 °C/4 h (conventional method). Conductivity data are given in Table 1.

ratio of the actual conductivity of a porous SDC sample to that of the conductivity of the dense sample. The conductivity of the dense sample was 0.071 S cm^{-1} at 800 °C, which is approximately twice that of the sample with 33.5% porosity made by the conventional process (Fig. 4). The conductivity of the sample with 51.2% porosity made by the conventional process (Fig. 5), however, is only about 4.31×10^{-4} S cm^{-1} at 800 °C. Conductivity of this sample is much lower than can be rationalized on the basis of a simple phenomenological equation, namely

$$\sigma_{\text{porous}} \approx \sigma_{\text{dense}}(1 - V_{\text{v}}) \tag{33}$$

It is readily seen that Eq. (33) is not applicable to the sample with 51.2% porosity made by conventional sintering. Note that interparticle necks are well developed in the sample with 33.5% porosity (Fig. 4) as compared to the sample with 51.2% porosity (Fig. 5). Also, the particle size is much smaller in the more porous sample.

Porous samples fabricated by leaching Ni + SDC cermets with porosity ranging between 31.2% and 54.8% exhibited conductivity values ranging between 0.05 and 0.0328 S cm^{-1}; that is the sample with 54.8% porosity exhibited a conductivity of ~0.0328 S cm^{-1} and the sample with 31.2% porosity exhibited a conductivity of 0.05 S cm^{-1}. Using Eq. (33), the estimated conductivities of the samples with 31.2% and 54.8% porosity are respectively 0.048 and 0.032 S cm^{-1}. These values are very close to the measured values on this second group of porous samples indicating the applicability of Eq. (33) to these samples.

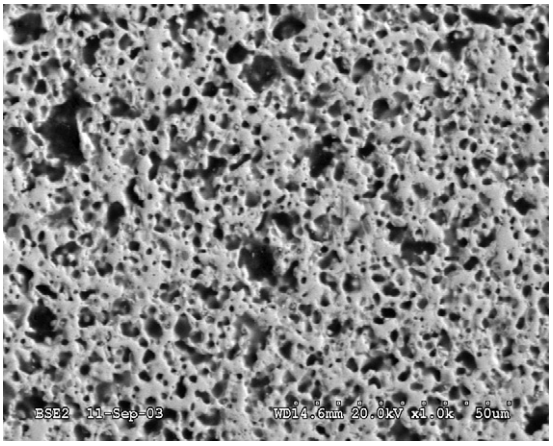

Fig. 6. An SEM micrograph of a Sm_2O_3-doped ceria (SDC) sample (porosity = 31.2%) sintered at 1600 °C/2 h (method comprising the fabrication of SDC + NiO composite, reduction of NiO to Ni, and its removal by leaching). Conductivity data are given in Table 2.

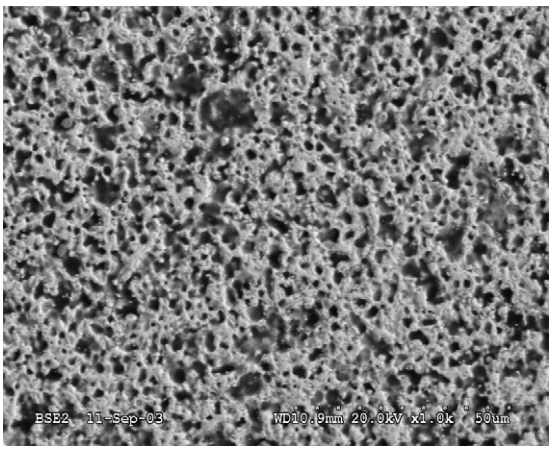

Fig. 7. An SEM micrograph of a Sm_2O_3-doped ceria sample (porosity = 39.7%) sintered at 1600 °C/2 h (method comprising the fabrication of SDC + NiO composite, reduction of NiO to Ni, and its removal by leaching). Conductivity data are given in Table 2.

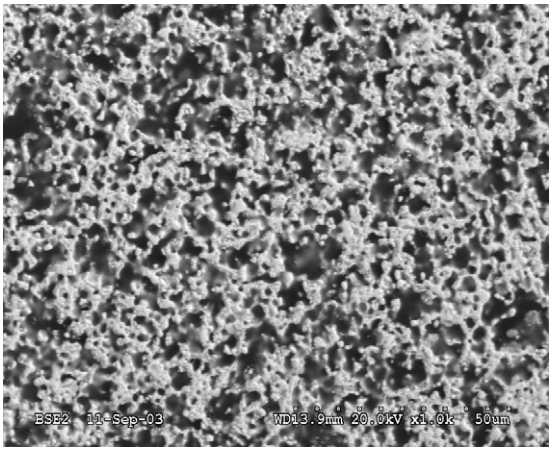

Fig. 8. An SEM micrograph of a Sm_2O_3-doped ceria sample (porosity = 54.8%) sintered at 1600 °C/2 h (method comprising the fabrication of SDC + NiO composite, reduction of NiO to Ni, and its removal by leaching). Conductivity data are given in Table 2.

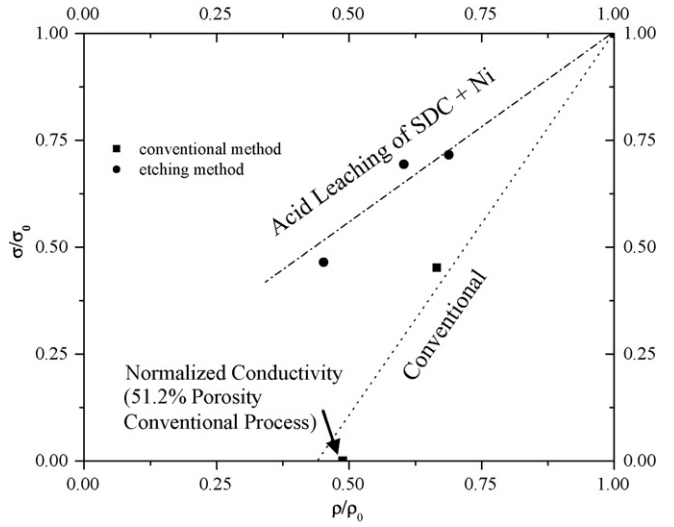

Fig. 9. Relative conductivity vs. relative density. The relative conductivity is defined as the ratio of the conductivity of a sample with a given porosity to that of the fully sintered (negligible porosity) sample. Similarly, the relative density is the ratio of density of a sample with a given porosity to that of a fully dense sample. The arrow shows the normalized conductivity of the conventionally sintered sample with 51.2% porosity having narrow necks. Its value is ~0.01 and thus appears to be close to the *x*-axis.

Fig. 8 shows an SEM micrograph of the sample with 54.8% porosity made by leaching Ni out Ni + SDC cermets. Note that inter-particle necks are well developed and the neck size is broad despite high porosity. The conductivity value of this sample is almost two orders of magnitude higher than the sample with about the same porosity (Fig. 5) but fabricated using the conventional method (Tables 1 and 2, and Fig. 9). This result shows that conductivity depends not only on porosity, but also on other microstructural parameters, such as grain size and neck size. Usually only when the grain size is small (on the order of a micron or lower), the grain boundary effects dominate the conductivity of polycrystalline ionic conductors. For samples with grain size on the order of several microns, the grain boundary effect may be measurable, but not dominant at high temperatures. Especially in doped ceria, it has been observed that the grain boundary effect is small (a few percent of the grain resistance) at 800 °C in dense materials with grain size on the order of a few microns [10]. Therefore, the large difference in conductivity of the two groups of samples with ~50% porosity must be primarily related to the differences in neck sizes, i.e., the connectivity (inter-particle neck size) has a significant effect on the conductivity of porous ionic conductors. While no direct measurements of inter-particle neck sizes are available, microstructures in Figs. 6–8 are consistent with narrow inter-particle neck sizes. The experimental results are thus in accord with the analytical expression given in Eq. (1) (or Eq. (B-13) which includes space charge effects) which describes effective resistivity as a function of neck size. That is, porous samples sintered by the conventional method exhibit relatively small neck sizes compared to those fabricated by the acid leaching of Ni + SDC cermets.

4.4. Resistivity of bulk and space charge layer as a function of oxygen partial pressure

Fig. 10 shows the calculated defect concentrations (on a log scale) inside the grain as a function of distance from the grain boundary core using the following parameters: $T = 600\,^{\circ}\mathrm{C}$, space charge potential $\Delta\phi(0) = 0.4\,\mathrm{V}$ [22], doping level = 10% ($[A']_b$) (corresponding $[V_O^{\bullet\bullet}]_b = 1.34 \times 10^{21}\,\mathrm{cm}^{-3}$), $p_{O_2} = 10^{-10}$ atm (corresponding $n_b = 3.18 \times 10^{15}\,\mathrm{cm}^{-3}$). Note that in the space charge layer the oxygen vacancy concentration increases and the electron concentration decreases as a function of distance from the grain boundary core into the grain; that is, oxygen vacancy concentration decreases and electron concentration increases when approaching the grain boundary from within the grain. Fig. 11 shows the calculated defect concentrations (on a log scale) inside the grain as a function of distance from the grain boundary core using the following parameters: $T = 800\,^{\circ}\mathrm{C}$, space charge potential, $\Delta\phi(0) = 0.4\,\mathrm{V}$, doping level = 10% (corresponding $[V_O^{\bullet\bullet}]_b = 1.34 \times 10^{21}\,\mathrm{cm}^{-3}$) and $p_{O_2} = 10^{-10}$ atm (corresponding $n_b = 1.02 \times 10^{18}\,\mathrm{cm}^{-3}$). Note that the lines for oxygen vacancy concentration and electron concentration cross at ζ (distance from grain boundary core) = 0.1 nm. When $\zeta < 0.1$ nm the so-called "inversion layer" is formed [22]. If the inversion layer is dominant in the space charge layer, the phenomenon of the space charge layer conductivity being higher than that of the bulk will be observed in very fine-grained materials. More specifically, when the electron conductivity in the space charge layer is higher than oxygen ion conductivity in the space charge layer, very fine-grained materials will exhibit predominantly electronic conduction.

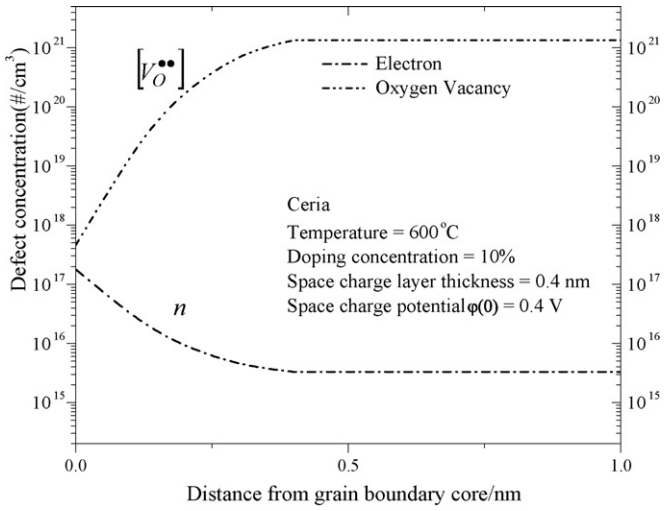

Fig. 10. Calculated defect concentrations (on a log scale) inside the grain as a function of distance from grain boundary core at 600 °C at a $p_{O_2} = 10^{-10}$ atm.

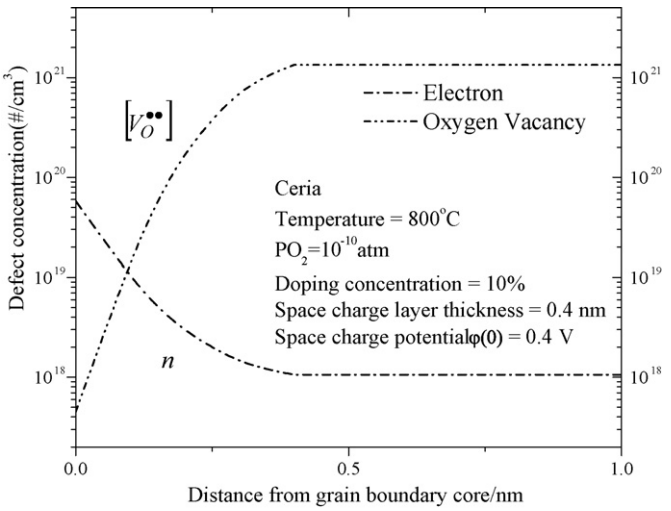

Fig. 11. Calculated defect concentrations (on a log scale) inside the grain as a function of distance from grain boundary core at 800 °C at a $p_{O_2} = 10^{-10}$ atm.

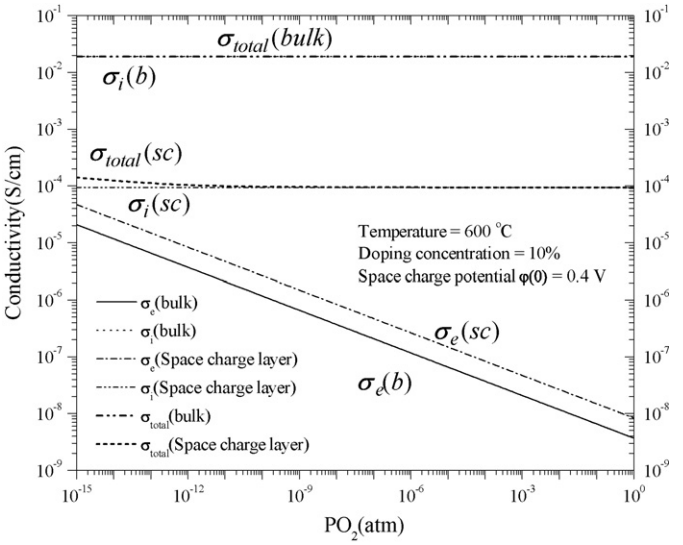

Fig. 12. Calculated ionic conductivity, electronic conductivity and total conductivity (on a log scale) in bulk and space charge layer as a function of various oxygen partial pressures. Temperature = 600 °C.

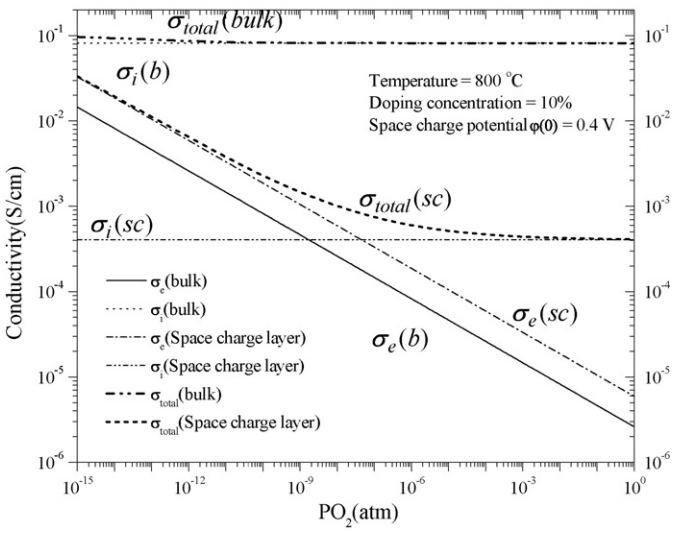

Fig. 13. Calculated ionic conductivity, electronic conductivity and total conductivity (on a log scale) in bulk and space charge layer as a function of various oxygen partial pressures. Temperature = 800 °C.

Fig. 12 shows the calculated ionic, electronic and total conductivity (ionic plus electronic) in the bulk and the space charge layer as a function of oxygen partial pressure using the following parameters: $T = 600\,^{\circ}C$, space charge potential, $\Delta\phi(0) = 0.4\,V$, doping level = 10 mol.%. Note that in the bulk and in the space charge layer, the electronic conductivity increases about 3–4 orders of magnitude when the p_{O_2} is decreased from 1 atm to 10^{-15} atm. However the ionic conductivity for all cases remains independent of p_{O_2} since it is dictated by the doping level. The ionic conductivity is greater than the electronic conductivity in both the bulk and the space charge layer. Also the ionic conductivity dominates the total conductivity over the p_{O_2} range from 10^{-15} atm and 1 atm. Thus, a fully dense material behaves as a purely ionic conductor over the entire range, regardless of the grain size. The space charge layer thickness is ~0.5 nm. Thus, including the two opposite faces of a grain, the total space charge layer thickness is ~1 nm. The ionic conductivity in the space charge layer is ~1/200th that in the bulk. Thus, for a material with a grain size on the order of 200 nm, there will be approximately equal contributions from the bulk and the space charge layer to the net ionic resistance. For samples with much larger grains, the space charge layer has negligible effect on the ionic resistance (at 600 °C and higher). However, for samples with much smaller grains (on the order of fractions of micron or less), and at low temperatures, the ionic resistance will be largely dominated by the space charge layer.

Fig. 13 shows the calculated ionic, electronic and total conductivity (ionic plus electronic) in the bulk and the space charge layer as a function of oxygen partial pressure using the following parameters: $T = 800\,^{\circ}C$, space charge potential, $\Delta\phi(0) = 0.4\,V$, and doping level = 10 mol.%. Note that at 800 °C, the average electronic conductivity in the space charge layer is greater than the average ionic conductivity in the space charge layer for $p_{O_2} < 10^{-7.6}$ range. This is due to the higher electron concentration at higher temperature and lower oxygen partial pressures. Also, the average electronic conductivity in the space charge layer is greater than the average electronic conductivity in the bulk. This is due to the excess electron concentration in the space charge layer. Note however that over the p_{O_2} range of the calculations (10^{-15} atm to 1 atm), the bulk ionic conductivity is greater than the electronic conductivity. At a p_{O_2} of 10^{-15} atm, the ionic conductivity is about ~7 times that of bulk electronic conductivity. A fully dense material at this low p_{O_2} (and at lower p_{O_2}) will be a mixed ionic-electronic conductor. The total bulk conductivity which is the sum of bulk ionic and bulk electronic conductivities increases with decreasing p_{O_2} below 10^{-11} atm. For p_{O_2} much lower than 10^{-15} atm, predominant conduction will be by electrons.

For samples with a very fine grain size (on the order of a few nanometers in size) the space charge layer will dominate conduction behavior at low p_{O_2} and at 800 °C. For a sample of ~2 nm grain size, the space change layer completely dominates conduction behavior. Note that below about $p_{O_2} \sim 10^{-9}$ atm, the predominant transport will be by electrons (governed by the space charge layer). Thus, fine-grained materials will exhibit predominantly electronic conduction. Indeed, it is well known that many ceria-based materials exhibit greater (relative) electronic conductivity if the grain size is in the nanometer range [21].

4.5. Effect of space charge on conduction: comparison between dense and porous ceria

The preceding sections described the results of calculations on the effect of space charge and morphology on conduction through porous and dense ceria. Equations given in Appendix B were numerically solved to determine the conductivity of porous SDC as a function of grain size and θ, neck size (Fig. 2). As seen in Fig. 2, small grains and narrow necks have a profoundly adverse effect on conductivity. Figs. 10 and 11 give calculated ionic and electronic defect concentrations as functions of distance from grain boundary for two temperatures at a $p_{O_2} = 10^{-10}$ atm. These results in principle can be used to estimate conductivities of samples of any grain size for $d \geq 2\lambda^*$. A better insight into the role of space charge, however, can be gained by comparing the effect of space charge on dense and porous materials. Simple calculations that compare dense and porous bodies are described below.

Consider a dense SDC sample of grain size d. Assuming much of the grain boundary resistance is due to the space charge layer of thickness λ^*, the net ionic resistivity of polycrystalline SDC is given by

$$\rho_p \approx \rho_g + \frac{2\rho_{sc}\lambda^*}{d} \tag{34}$$

which assumes a simple brick-layer type model. At 600 °C in air, for a grain size of 1 μm (radius $R = 0.5$ μm), the estimated resistiv-

ity of a polycrystalline material is $\rho_p \approx 60.48\,\Omega$ cm, of which the contribution from the bulk grains is $\rho_g \approx 52\,\Omega$ cm. Thus, 8.48 Ω cm is attributed to the space charge layer, which means ~14% of the total resistivity is due to the space charge layer. For the simplified calculations of the space charge layer on porous bodies, we will use Eq. (1) with $\rho_{gb}\delta_{gb}$ replaced by $\rho_{sc}\lambda^*$ and ignoring the rest of the contributions (given Eq. (B-13)). Thus, we will use the simplified equation:

$$\rho_{eff} \approx \frac{2\rho_g}{\pi\sqrt{1-\alpha^2}} \ln\left[\frac{1+\sqrt{1-\alpha^2}}{1-\sqrt{1-\alpha^2}}\right] + \frac{2\rho_{sc}\lambda^*}{\pi R\alpha^2\sqrt{1-\alpha^2}} \quad (35)$$

to estimate the resistivity of a porous material. For the same parameters as above for angle $\theta = 5^\circ$ that is $\alpha = r_0/R = \sin\theta = 0.08716$, the first term in Eq. (35) is 416 Ω cm while the second term in Eq. (35) is 1427 Ω cm for a total resistivity $\rho_{eff} = 1843\,\Omega$ cm. Thus, the total resistivity of the porous body with narrow necks is 1843/60.48 times or over 30 times that of the resistivity of the fully dense material. Also, note that ~77% of the net resistivity in the porous materials is attributable to the space charge layer. Note a very large effect of space charge, despite a very thin space charge layer, due to a significant depletion of oxygen vacancy concentration near grain boundaries. Because of the constriction (narrow necks), the space charge layer has a much stronger adverse effect on transport through porous materials as compared to fully dense materials. These conclusions have important implications concerning SOFC cathodes, mixed ionic-electronic conducting (MIEC) membranes with surface porous layers, and other devices with porous surface layers.

4.6. Calculations and experimental results on the effective conductivity of porous SDC as a function of temperature and oxygen partial pressure

Fig. 14 shows the calculated effective conductivity of porous SDC as a function of oxygen partial pressure at various temperatures for grain size = 2.5 μm, $\theta = 18^\circ$ (a measure of the relative neck size) and porosity = 30% over an oxygen partial pressure range between 10^{-15} atm and 1 atm. Note that at 600 °C the conductivity is essentially independent of p_{O_2} over the range investigated. This is attributed to the predominant ionic conduction which is dictated by the dopant concentration. At 800 °C the effective conductivity increases from 0.02 S cm^{-1} to 0.033 S cm^{-1} with a decrease of p_{O_2} from 1 atm to 10^{-15} atm. The difference (0.013 S cm^{-1}) is due to electronic conduction at low p_{O_2}.

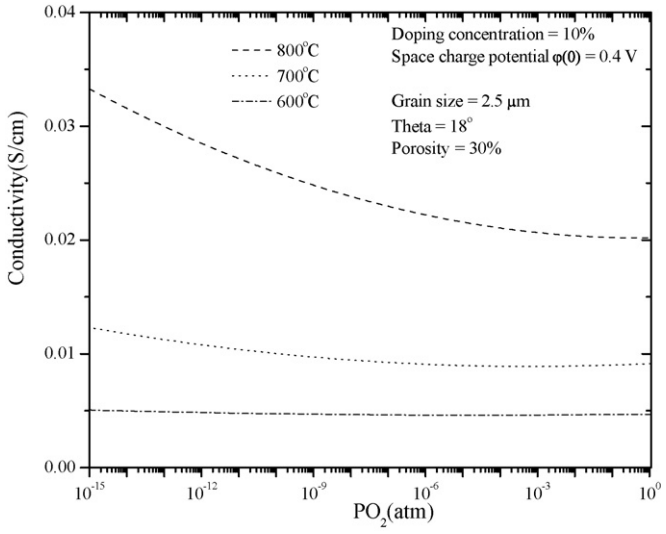

Fig. 14. Calculated total conductivity, ionic + electronic, as a function of oxygen partial pressure and temperature.

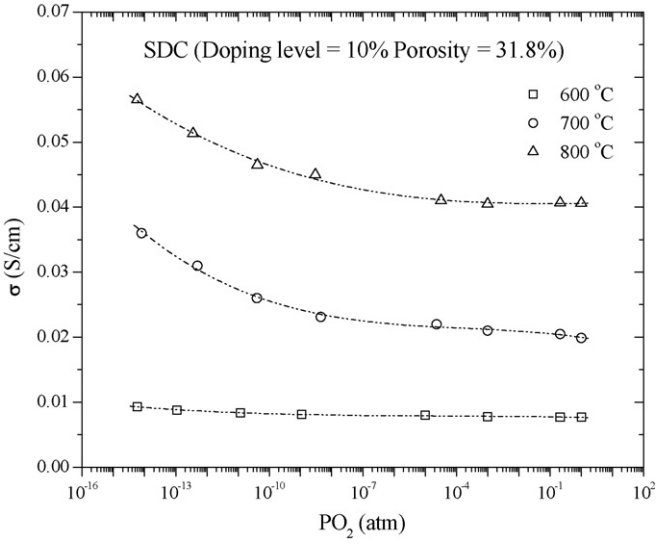

Fig. 15. Measured electrical conductivity (on a log scale) by a DC four-probe technique as a function of oxygen partial pressure and temperature.

Fig. 15 shows the measured effective conductivity of porous SDC as a function of oxygen partial pressure at 600 °C, 700 °C, and 800 °C. Note that the experimental data show very similar trends and the quantitative agreement is also quite good. Considering that no adjustable parameters were used, all calculations are based on previously reported information in the literature, and some of the data used in the calculations are on ceria containing dopants other than Sm_2O_3 (e.g. Gd_2O_3), the agreement between the experimental results and model calculations is actually quite good. In this work the lowest p_{O_2} at which measurements were made was 10^{-15} atm. For p_{O_2} lower than 10^{-15} atm, rapid rise in total conductivity is expected because of enhanced electronic conduction as is well known in ceria [31].

5. Summary

A simple analytical equation which describes conductivity of porous materials in terms of particle size and inter-particle neck size is presented. The equation demonstrates the profound role of inter-particle contact on conductivity. At very small neck sizes, the conductivity sharply decreases (resistivity increases). The implications are that the effective resistivity of porous bodies may be very high in poorly sintered materials. In order to experimentally demonstrate the role of inter-particle contact, porous Sm_2O_3-doped ceria (SDC) samples were fabricated by two methods. (1) a conventional method consisting of sintering of powder compacts and (2) sintering of two-phase NiO + SDC powder compacts to near theoretical density, reduction of NiO to Ni in hydrogen at 800 °C, and acid leaching of Ni at room temperature to fabricate porous SDC samples. The former approach led to porous SDC samples of narrow necks, especially those with relatively high porosity (~50%). The latter approach led to porous SDC samples with large neck sizes. Four-probe DC conductivity was measured in air at 800 °C. For samples of ~50% porosity, the acid leached samples exhibited up to two orders of magnitude higher conductivity as compared to conventionally sintered samples. The large difference in conductivities was attributed to the relative differences in neck sizes with some difference also attributed to differences in grain sizes.

The model also included the role of space charge on conductivity in dense and porous SDC samples. For fully dense samples

of grain size on the order of a micron or more, and temperatures greater than 600 °C, the role of space charge is relatively modest. By contrast, the role of space charge is much larger in porous materials, and especially those with narrow inter-particle necks. This result has important implications in devices which use of porous materials, such as electrodes in electrochemical devices.

Calculations were performed on porous SDC as a function of temperature (600–800 °C) and oxygen partial pressure (10^{-15} atm to 1 atm). The calculations show that at 600 °C samples exhibit predominantly ionic conduction over the p_{O_2} range 10^{-15} atm to 1 atm. At 800 °C, significant electron conduction occurs at low p_{O_2}. The total conductivity of porous SDC was measured over a temperature range from 600 °C to 800 °C and a p_{O_2} range from 10^{-15} atm to 1 atm. The experimental data are in good agreement with the predictions of the model.

Acknowledgements

This work was supported at the University of Utah in part by the US Department of Energy under Contract No. DE-FC26-02NT41602 and in part by the DOE EFRC Grant No. DE-SC0001061 as a flow through from the University of South Carolina.

Appendix A.

Fig. 1(a) and (b) shows the geometry of the particle used for calculations.

For region I, the resistance for the range between $x = x_0$ and $x = R$, is given by

$$R_I = \int dR_I = \frac{\rho_g}{\pi}\int_{x_o}^{R}\frac{dx}{\left[R^2-(R-x)^2\right]} = \frac{\rho_g}{\pi}\int_0^R \frac{dx}{x(2R-x)}$$
$$= \frac{\rho_g}{2R\pi}\int_{x_0}^{R}\left\{\frac{dx}{x}+\frac{dx}{(2R-x)}\right\} \quad \text{(A-1)}$$

$$R_I = \left[-\frac{\rho_g}{2\pi R}\ln\left(\frac{2R-x}{x}\right)\right]_{x=x_0}^{x=R} = -\frac{\rho_g}{2\pi R}\ln\left(\frac{2R-x_0}{x_0}\right) \quad \text{(A-2)}$$

where $\alpha = r_0/R$ and

$$x_0 = R-\sqrt{R^2-r_0^2} = R-R\sqrt{(1-\alpha^2)} \quad \text{(A-3)}$$

Thus

$$R_I = \frac{\rho_g}{2\pi R}\ln\left[\frac{1+\sqrt{1-\alpha^2}}{1-\sqrt{1-\alpha^2}}\right] \quad \text{(A-4)}$$

For region II corresponding to transport across the grain boundary core, R_{II} is given by

$$R_{II} = R_{gb} = \frac{\rho_{gb}\delta_{gb}}{2\pi r_0^2} \quad \text{(A-5)}$$

$$R_{eff} = R_I + R_{II} \quad \text{(A-6)}$$

Stacking cut spheres one on top of the other and arranging them on a square lattice gives

$$\rho_{eff} \approx \frac{4R_{eff}R^2}{R-x_0} = \frac{4R_{eff}R}{\cos\theta} \quad \text{(A-7)}$$

which gives

$$\rho_{eff} \approx \frac{2\rho_g}{\pi\sqrt{1-\alpha^2}}\ln\left[\frac{1+\sqrt{1-\alpha^2}}{1-\sqrt{1-\alpha^2}}\right] + \frac{2\rho_{gb}\delta_{gb}}{\pi R\alpha^2\sqrt{1-\alpha^2}} \quad \text{(A-8)}$$

Appendix B.

Fig. 1(c) shows the geometry of the particle used for calculations.

For region I, corresponding to the net resistance for the range between $x = x_0 + \lambda^*$ and $x = R$:

$$y = \sqrt{2Rx-x^2} = R\sin\theta \quad \text{(B-1)}$$

$$x = R - R\cos\theta \quad \text{and} \quad dx = R\sin\theta\, d\theta \quad \text{(B-2)}$$

Note that

$$\Delta y = \frac{\lambda^*}{\sin\theta} \quad \text{and} \quad \sin\theta = \frac{y}{R} = \frac{\sqrt{2Rx-x^2}}{R} \quad \text{(B-3)}$$

Then one can show that

$$y_g = y - \Delta y = R\sin\theta - \frac{\lambda^*}{\sin\theta} \quad \text{(B-4)}$$

Thus,

$$\pi(y^2-y_g^2) = \pi(y^2-(y-\Delta y)^2) = \pi\left(2R\lambda^* - \frac{\lambda^{*2}}{\sin^2\theta}\right) \quad \text{(B-5)}$$

In the bulk and space charge parallel regions:

$$\frac{1}{dR_I} = \frac{1}{\frac{\rho_g dx}{\pi y_g^2}} + \frac{1}{\frac{\rho_{sc}dx}{\pi(y^2-y_g^2)}} \quad \text{(B-6)}$$

Thus,

$$dR_I = \frac{\rho_g\rho_{sc}R\sin^3\theta\, d\theta}{\pi(2R\lambda^*\sin^2\theta-\lambda^{*2})\rho_g + \pi(R\sin^2\theta-\lambda^*)^2\rho_{sc}} \quad \text{(B-8)}$$

The integration of Eq. (B-8) from $x = x_0 + \lambda^*$ to $x = R$, i.e., from $\theta = \cos^{-1}((R-x_0-\lambda^*)/R)$ to $\theta = \pi/2$, gives

$$R_I = \int_{\cos^{-1}\left(\frac{R-x_0-\lambda^*}{R}\right)}^{\frac{\pi}{2}} \frac{\rho_g\rho_{sc}R\sin^3\theta d\theta}{\pi(2R\lambda^*\sin^2\theta-\lambda^{*2})\rho_g + \pi(R\sin^2\theta-\lambda^*)^2\rho_{sc}} \quad \text{(B-9)}$$

In region II, corresponding to the net resistance for the range $x = x_0$ to $x = x_0 + \lambda^*$:

$$dR_{II} = \frac{\rho_{sc}dx}{\pi y^2} = \frac{\rho_{sc}R\sin\theta\, d\theta}{\pi(R\sin\theta)^2} = \frac{\rho_{sc}d\theta}{\pi R\sin\theta} \quad \text{(B-10)}$$

The integration of Eq. (B-10) between $x = x_0$ to $x = x_0 + \lambda^*$, i.e., from $\theta = \cos^{-1}((R-x_0)/R)$ to $\theta = \cos^{-1}((R-x_0-\lambda^*)/R)$, gives

$$R_{II} = \int_{\cos^{-1}\left(\frac{R-x_0}{R}\right)}^{\cos^{-1}\left(\frac{R-x_0-\lambda^*}{R}\right)} \frac{\rho_{sc}d\theta}{\pi R\sin\theta} \quad \text{(B-11)}$$

For region III corresponding to the transport across the grain boundary core, R_{III} is given by

$$R_{III} = R_{gb} = \frac{\rho_{gb}\delta_{gb}}{\pi r_0^2} = \frac{\rho_{gb}\delta_{gb}}{\pi(R\sin\theta)^2} \quad \text{(B-12)}$$

From Eqs. (B-9), (B-11) and (B-12), it is apparent that if x_0 and λ^* are known, $\cos^{-1}((R-x_0)/R)$ and $\cos^{-1}((R-x_0-\lambda^*)/R)$ can be calculated. Thus, R_I, R_{II} and R_{III} can be calculated. The effective resistance then is given by

$$R_{eff} = R_I + R_{II} + R_{III} \quad \text{(B-13)}$$

The preceding calculations tacitly assume predominantly ionic conduction through all regions such that $\rho_i \ll \rho_e$. If such is not the case, then two sets of calculations need to be performed; one to obtain the effective ionic resistance given by

$$R_{eff(i)} = R_{I(i)} + R_{II(i)} + R_{III(i)} \quad \text{(B-14)}$$

and the other to obtain the effective electronic resistance given by

$$R_{\mathrm{eff(e)}} = R_{\mathrm{I(e)}} + R_{\mathrm{II(e)}} + R_{\mathrm{III(e)}} \tag{B-15}$$

The net effective resistance is then given by

$$R_{\mathrm{eff}} \approx \frac{R_{\mathrm{eff(i)}} R_{\mathrm{eff(e)}}}{(R_{\mathrm{eff(i)}} + R_{\mathrm{eff(e)}})} \tag{B-16}$$

In the present work, this aspect was neglected and electronic and ionic contributions were incorporated using Eqs. (15) and (28) directly into Eq. (B-13). At low p_{O_2} with significant electronic conduction, this is expected to introduce some error.

References

[1] J.W. Kim, A.V. Virkar, K.-Z. Fung, K. Metha, S.C. Singhal, J. Electrochem. Soc. 146 (1999) 69.
[2] P. Jasinski, T. Suzuki, H.U. Anderson, Sens. Actuators B 95 (2003) 73–77.
[3] H.J. Beie, A. Gnorich, Sens. Actuators B 4 (1991) 393–399.
[4] A.D. Brailsford, D.K. Hohnke, Solid State Ionics 11 (1983) 133.
[5] M. Kleitz, L. Dessemond, M.C. Steil, Solid State Ionics 75 (1995) 07.
[6] C. Tian, S.-W. Chan, Solid State Ionics 134 (2000) 89–102.
[7] J.-H. Hwang, D.S. McLachlan, T.O. Mason, J. Electroceram. 3 (1999) 7–16.
[8] Y.-M. Chiang, E.B. Lavik, D.A. Blom, Nanostruct. Mater. 9 (1997) 633.
[9] K. El Adham, A. Hammou, Solid State Ionics 9&10 (1983) 905–912.
[10] S.J. Hong, K. Mehta, A.V. Virkar, J. Electrochem. Soc. 145 (1998) 638.
[11] R. Gerhardt, A.S. Nowick, J. Am. Ceram. Soc. 69 (1986) 641–646.
[12] J. Tanaka, J.-F. Baumard, P. Abelard, J. Am. Ceram. Soc. 70 (1987) 637–643.
[13] G.M. Christie, F.P.F. van Berkel, Solid State Ionics 83 (1996) 17–27.
[14] J. Frenkel, Kinetic Theory of Liquids, Dover Publications, Dover, NY, 1946, p. 37.
[15] K. Lehovec, J. Chem. Phys. 21 (7) (1953) 1123–1128.
[16] K.L. Kliewer, J.S. Koehler, Phys. Rev. 140 (4A) (1965) A1226–A1240.
[17] X. Guo, Solid State Ionics 81 (1995) 235–242.
[18] X. Guo, Solid State Ionics 99 (1997) 137–142.
[19] S. Kim, J. Maier, J. Electrochem. Soc. 149 (2002) 10.
[20] A. Tschöpe, E. Sommer, R. Barringer, Solid State Ionics 139 (2001) 255.
[21] A. Tschöpe, Solid State Ionics 139 (2001) 267.
[22] X. Guo, W. Sigle, J. Maier, J. Am. Ceram. Soc. 86 (2003) 77–87.
[23] A. Tschöpe, C. Bäuerle, R. Birringer, J. App. Phys. 95 (2004) 1204.
[24] I. Lubomirsky, J. Fleig, J. Maier, J. App. Phys. 92 (2002) 6819.
[25] J. Maier, Ber. Busenges. Phys. Chem. 90 (1986) 26.
[26] H.L. Tuller, A.S. Nowick, J. Electrochem. Soc. 126 (1979) 209.
[27] D. Scheider, M. Gödickemeier, L.J. Gauckler, J. Electroceram. 1 (1997) 165.
[28] D.Y. Wang, A.S. Nowick, J. Solid State Chem. 35 (1980) 325.
[29] R. Gerhardt, A.S. Nowick, J. Am. Ceram. Soc. 69 (1986) 641.
[30] H.L. Tuller, in: T.O. Sørensen (Ed.), Nonstoichiometric Oxides, Academic Press, New York, 1981, p. 271.
[31] S. Wang, T. Kobayashi, M. Dokiya, T. Hashimoto, J. Electrochem. Soc. 147 (10) (2000) 3606–3609.
[32] X. Guo, J. Maier, J. Electrochem. Soc. 148 (2001) E121.
[33] D.Y. Wang, D.S. Park, J. Griffith, A.S. Nowick, Solid State Ionics 2 (1981) 95.